XXXX

Analysis of the Seismic Fragility of Rocking Bridges Based on SMA Ring Springs and ECC Material

Baixian Fu[1], Xian'gang Liu[2], Jinglin Zhou[2], Haifeng Shi[3], Chao Xie[4], Qiuyue Li[4], Yuxiao Wang[5*]

[1] Shandong Hi-speed Co., Ltd., Ji'nan 25014, Shandong Province, China;
[2] Guiyang Highway Bureau, Guiyang 550001, Guizhou Province, China;
[3] Wudang Highway Management Section, Guiyang 550018, Guizhou Province, China;
[4] Guizhou Qingzhen Highway Management Section, Guiyang 551499, Guizhou Province, China;
[5] Dept. of Bridge Engineering, Tongji University, Shanghai 200092, China.
* Correspondence: wong_reshaw@tongji.edu.cn

Abstract: To achieve a graded seismic protection objective, namely, no damage under minor earthquakes, repairable damage under moderate earthquakes, and replaceable damage under major earthquakes, a novel rocking bridge system based on shape memory alloy (SMA) ring springs is proposed in this study. A constitutive model of the SMA ring springs is first developed and implemented in open-source finite element software OpenSees. An iterative design procedure for rocking piers is subsequently proposed, in which the slip ratio is adopted as an optimization index for the geometric configuration of the rocking piers. A typical bridge is then selected as a case study example. Finite element models of both a conventional bridge and an engineered cementitious composite (ECC) rocking bridge are subsequently established in OpenSees, and the seismic fragility of the two bridge systems is analyzed. The results indicate that the self-locking mechanism of the SMA ring springs effectively controls the rocking amplitude of the piers, thereby ensuring safe and reliable performance. Compared with conventional bridges, rocking bridges exhibit superior seismic performance and lower seismic fragility.

Keywords: seismic response; SMA ring springs; ECC rocking piers; fragility analysis

Citation: Baixian Fu, Xian'gang Liu, Jinglin Zhou, et al. Analysis of the Seismic Fragility of Rocking Bridges Based on SMA Ring Springs and ECC Material[J]. Prestress Technology, DOI: 10.59238/j.pt.XXXX.XX.001. Published: XX/XX/XXXX

Publisher's Note: Prestress technology stays neutral with regard to jurisdictional claims in published maps and institutional affiliations.

Scientific Research

1 Introduction

China is located between the Circum-Pacific Seismic Belt and the Eurasian Seismic Belt. According to the Seismic Ground Motion Parameter Zonation Map of China published by the China Earthquake Administration in 2015, nearly 27.4% of the land area of China is subject to seismic intensity levels of VII or above. Thirty provinces, municipalities, and autonomous regions in mainland China have experienced destructive earthquakes of magnitude 6.0 or greater. Until the end of the last century, most seismic design codes for bridges worldwide encompassed a force-based design approach [1-2]. Postearthquake damage investigations following the Loma Prieta (1989), Northridge (1994), Kobe (1995), and Wenchuan (2008) earthquakes revealed that numerous bridges were severely damaged or exhibited excessive residual deformation that was difficult to repair. This restriction severely impeded postearthquake rescue operations and resulted in substantial economic losses and casualties. Adopting the Wenchuan earthquake as an example [3], a seismic damage survey of 1,657 highway bridges in severely affected areas (national and provincial trunk roads) indicated that 8.2% of the surveyed bridges were either completely or severely damaged. In response, the earthquake engineering community reevaluated the limitations of force-based design and subsequently proposed performance-based seismic design concepts. The governments of countries such as China and the United States have since issued design codes that are based on

displacement-based performance criteria [4-5], which aim to prevent bridge collapse by controlling the rotation capacity of plastic hinges, thereby achieving the design objective of ensuring no collapse under major earthquakes.

However, recent postearthquake investigations have revealed that reinforced concrete (RC) bridges commonly suffer excessive residual deformation. For example, after the 1995 Kobe earthquake, although many bridges did not collapse, more than 100 RC bridge piers with a permanent slip ratio exceeding 1.5% were demolished [6]. This condition has created an urgent need to fundamentally revise the seismic design objectives for bridge structures. Consequently, in many countries (e.g., the United States, Japan, and New Zealand), national seismic codes have been updated, thereby reevaluating the relative importance of ductility, load-carrying capacity, life safety, and functional recoverability [7-8]. Among the various solutions, rocking bridge piers have received significant interest among bridge engineers because of their high deformation capacity [9] and ease of prefabrication [9-12]. The concept of rocking piers conforms to the principles of seismic isolation and energy dissipation, as this design can substantially prolong the vibration period of the bridge structure, thereby reducing the seismic forces generated during earthquakes. Shake-table tests of posttensioned rocking piers [13] have demonstrated that such systems can experience large lateral displacements, with the maximum slip ratio at the pier top reaching 10%, while the residual displacement of the pier body remains lower than 0.5%. To enhance the seismic performance of rocking piers further, researchers have developed new self-centering components and energy dissipation devices, and their effectiveness has been extensively investigated [14-16].

Nevertheless, to date, rocking bridges have rarely been constructed worldwide. For example, Palermo A. et al. [17] added posttensioned prestressing tendons around the pier and pile cap to enable rocking under seismic loading; however, the energy dissipation capacity was limited, and the system could be activated even under service loads such as vehicle braking, thus affecting normal serviceability. In another example, rocking piers were adopted in the South Rangitikei Railway Bridge in New Zealand, which was completed in 1981 [18]. This rocking system comprised shear dowels, shear keys, rocking cushions, and torsional steel dampers for energy dissipation. Because the rocking system was installed within hollow tall piers, any damage incurred during an earthquake would be difficult to repair. Domestically, Han et al. [19] first designed a two-column rocking pier using unbonded prestressed steel strands combined with energy-dissipating steel plates and applied this design to a continuous girder bridge with a main span of 40 m in a seismic region.

Thus, while the use of posttensioned prestressing tendons and various energy-dissipating components can significantly reduce damage and provide adequate self-centering capability, postearthquake repair and replacement of damaged components remain time-consuming and costly tasks. More importantly, in the repair and replacement process, the bridge remains in a hazardous condition, especially under the influence of potential aftershocks, posing a risk of girder collapse. In addition, the relaxation of posttensioned prestressing strands is difficult to manage in practice. With the rapid advancement in material science, novel components and structural systems that are based on new materials offer new opportunities for seismic design of bridge engineering. For example, innovative bridge components and systems using nickel – titanium shape memory alloys (SMAs) have been widely applied in bridge seismic design [20]. The primary design philosophy of SMA components is to exploit the superelasticity of SMAs to increase both their self-centering capability and energy dissipation capacity. Varela and Saidi [21] investigated the seismic isolation and energy dissipation performance of RC bridge piers

 https://doi.org/10.59238/j.pt.XXXX.XX.001

by combining SMA bars in the plastic hinge region with elastomeric rubber pads. The results of this study revealed that under 250% of the design seismic load, the RC bridge piers exhibited almost no damage except for the buckling of the SMA bars. The first real-world application was the on-ramp bridge of State Route 99 in Seattle, Washington, USA, where SMA bars were uniformly arranged along the longitudinal direction in the plastic hinge region to increase seismic resilience [22]. It should be noted, however, that SMA bars are sensitive to manufacturing defects and are susceptible to unexpected fracture at high strains [23]. Although the pretensioning of SMA bars can prevent buckling, it also increases the risk of fracture and reduces the service life [24]. In addition, ring springs have been applied in several other contexts [25-26].

On the basis of the above considerations, the conditions and technical measures necessary for realizing rocking piers are carefully examined in this study. First, a new resilient seismic bridge system based on SMA ring – spring rocking piers is proposed. The working mechanism of the high-efficiency rocking pier and the method for establishing its finite element model are subsequently clarified. Furthermore, the seismic energy dissipation mechanism of the novel rocking bridge system is theoretically investigated, its seismic fragility is quantified, and a comparison with that of conventional bridges is conducted. Ultimately, this study provides theoretical and practical foundations for developing next-generation design codes for resilient seismic bridges.

2 Structural System of the Novel Rocking Bridge

To achieve rapid postearthquake functional recovery of bridges and realize the design philosophy of no damage under minor earthquakes, replaceable damage under moderate earthquakes, and repairable damage under major earthquakes, a novel rocking bridge system incorporating SMA ring springs is proposed. As shown in Figure 1, the system comprises mainly four sets of SMA ring springs and a rocking pier. The rocking interface is located between the upper and lower caps. Both the rocking pier and the caps are made of an engineered cementitious composite (ECC) material. In addition, to increase the durability of expansion joints, ECC material is applied in the anchorage zones. To ensure the integral behavior of the rocking bridge under normal service conditions and minor earthquakes, the SMA ring springs are precompressed to maintain close contact between the upper and lower caps, thereby ensuring cooperative action. Under minor earthquakes (with a 63% probability of exceedance in 50 years), all the components are designed to remain undamaged. Under moderate earthquakes (with a 10% probability of exceedance in 50 years), the horizontal slip ratio of the girder is permitted to be less than 1.0%, and damaged elements or components should be promptly replaced. Under major earthquakes (with a 2% probability of exceedance in 50 years), the horizontal slip ratio of the girder is permitted to be lower than 2.5%, and vulnerable components should be readily repairable.

2.1 SMA Ring Springs

SMA ring springs [27] constitute a type of compression spring assembled from multiple outer rings made of SMA with internal conical surfaces and inner rings made of precision steel with external conical surfaces. The inner and outer rings are assembled in an interlocking (embedded) manner, which facilitates easy disassembly and replacement. When subjected to vertical loading, the SMA outer rings expand radially, whereas the precision steel inner rings contract inward. With increasing radial stress, a substantial vertical resistance force is generated. Moreover, the friction between the inner and outer rings provides significant energy dissipation. The main configuration of the SMA ring springs is shown in Figure 2.

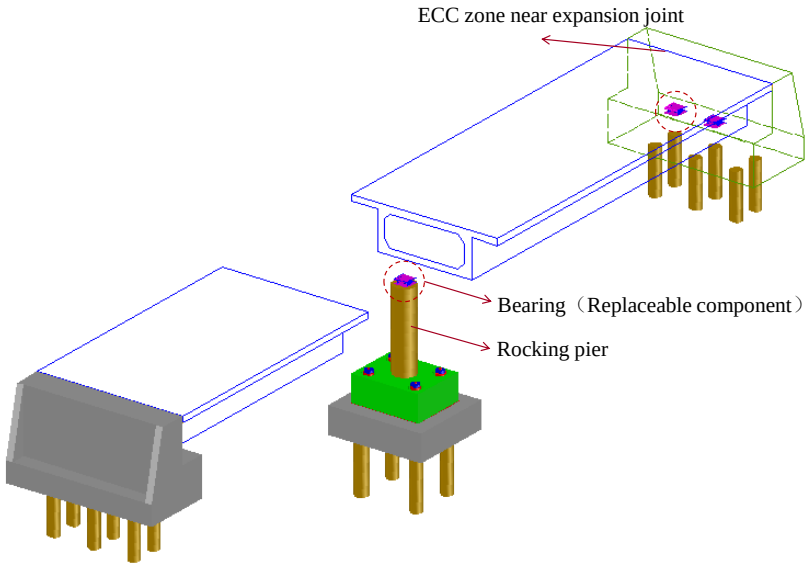

Figure 1 Rocking bridge structural system incorporating SMA ring springs

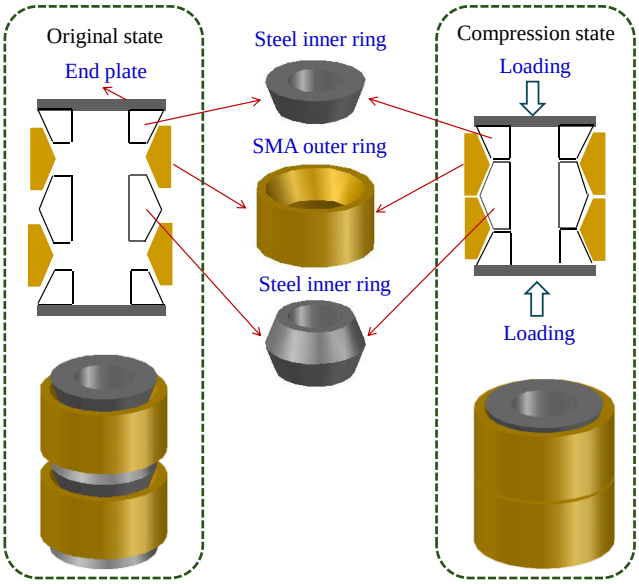

Figure 2 Configuration of the SMA ring springs

2.2 *Working Stiffness and Constitutive Model of SMA Ring Springs*

To establish a constitutive model of the SMA ring springs, an analytical expression for the working stiffness of the SMA ring springs is first derived. The objective is to preserve the key characteristics of the model while ensuring its practicality for engineering applications. The following three assumptions are made:

(1) Deformation of the inner rings is neglected;

(2) The hoop strain of the outer rings is limited to a specified range;

(3) The hoop stress is assumed to remain constant throughout the ring and uniformly distributed along the circumference.

With respect to Assumption 1, the high-strength steel inner rings are designed to remain within the elastic range, and their deformation is negligible compared with that of the SMA outer rings. With respect to Assumption 2, according to Wang et al. [27], when the stress level of the SMA outer rings exceeds a certain threshold, the recoverability of the material is significantly impaired. Therefore, to fully exploit the material, the strain in the SMA ring springs is limited to a certain range. With respect to Assumption 3, from a structural perspective, the thickness of the outer rings is very small relative to the diameter of the ring spring assembly. Conse-

 https://doi.org/10.59238/j.pt.XXXX.XX.001

quently, the hoop stress gradient along the thickness direction is not significant, and it is reasonable to assume a uniform stress throughout the ring. Moreover, because of the occurrence of axisymmetry, the hoop stress is considered uniformly distributed along the circumference such that the value at the centroid of the ring can represent the stress along the entire circumference. Thus, the applicability of the approximate stiffness solution is limited to cases in which the strain of the ring spring remains within the ultimate strain range and the thickness of the outer rings is small relative to the diameter.

As shown in Figure 3, considering a single layer of the ring spring subjected to vertical loading (during the loading phase), the vertical force equilibrium can be expressed as follows:

$$F = N\sin(\beta) + \mu N\cos(\beta) \tag{1}$$

where F is the external load, and N is the normal contact force at the conical interface. The horizontal component of the normal contact force N causes expansion of the SMA outer ring. Assuming that the SMA outer ring is expanded under the influence of a uniformly distributed force ρ_2 along its circumference, the following expression can be obtained:

$$2N\cos(\beta) = \rho_2 \pi D_c \tag{2}$$

where D_c is the equivalent diameter of the SMA outer ring based on the cross-sectional centroid. Considering the free-body diagram of a half-ring shown in Figure 3, the tensile force S in the cross section is balanced by the parallel component of the equivalent resultant of ρ_2 as follows:

$$2S = \int_0^{\pi} \rho_2 \sin(\alpha) \frac{D_c}{2} d\alpha \tag{3}$$

where S is the equivalent force at the centroid. Equation (3) can be further simplified as $S = \rho_2 D_c/2$. Considering $S = \sigma A$, where σ is the stress in the cross-section of the outer ring and A is the cross-sectional area of the outer ring, we can obtain the following:

$$\rho_2 = \frac{2\sigma A}{D_c} \tag{4}$$

Combining Equations (2) and (4), the normal contact force N at the conical interface can be expressed as follows:

$$N = \frac{\pi\sigma A}{\cos(\beta)} \tag{5}$$

Substituting Equation (5) into Equation (1) yields the following modified form of Equation (1):

$$F = \frac{\pi\sigma A}{\cos(\beta)}\sin(\beta) + \mu\frac{\pi\sigma A}{\cos(\beta)}\cos(\beta) = \pi\sigma A(\tan(\beta) + \mu) \tag{6}$$

Equation (6) can be used to establish the relationship between the external load applied to the ring spring and the hoop stress. Moreover, by considering the geometric relationships, the following relationship can be established between the radial deformation (δR) and the axial deformation (Δ) of the ring spring:

$$\tan(\beta) = \frac{\delta R}{\Delta} = \frac{\delta D}{2\Delta} \tag{7}$$

where δR and δD denote the radial deformation of the ring and the deformation of the ring diameter, respectively. The composition of the radial deformation δD is considered below.

$$\delta D = \frac{\sigma D}{E} \tag{8}$$

Combining Equation (6), the loading stiffness K can be obtained as follows:

$$K=\frac{F}{\Delta}=\frac{2\pi EA\tan(\beta)(\tan(\beta)+\mu)}{D} \tag{9}$$

Let $\gamma=\tan(\beta)+\mu$. The analytical expression of the loading stiffness can be simplified as follows:

$$K=\frac{2\pi EA\tan(\beta)\gamma}{D} \tag{10}$$

Similarly, at the unloading stage, the relative slip between the inner and outer rings occurs along the opposite direction to that at the loading stage, and the direction of the frictional force at the conical interface is reversed.

$$F=\frac{\pi\sigma A}{\cos(\beta)}\sin(\beta)-\mu\frac{\pi\sigma A}{\cos(\beta)}\cos(\beta)=\pi\sigma A(\tan(\beta)-\mu) \tag{11}$$

Therefore, the unloading stiffness can be expressed as follows:

$$K'=\frac{2\pi EA\tan(\beta)\gamma'}{D} \tag{12}$$

$$\gamma'=\tan(\beta)-\mu \tag{13}$$

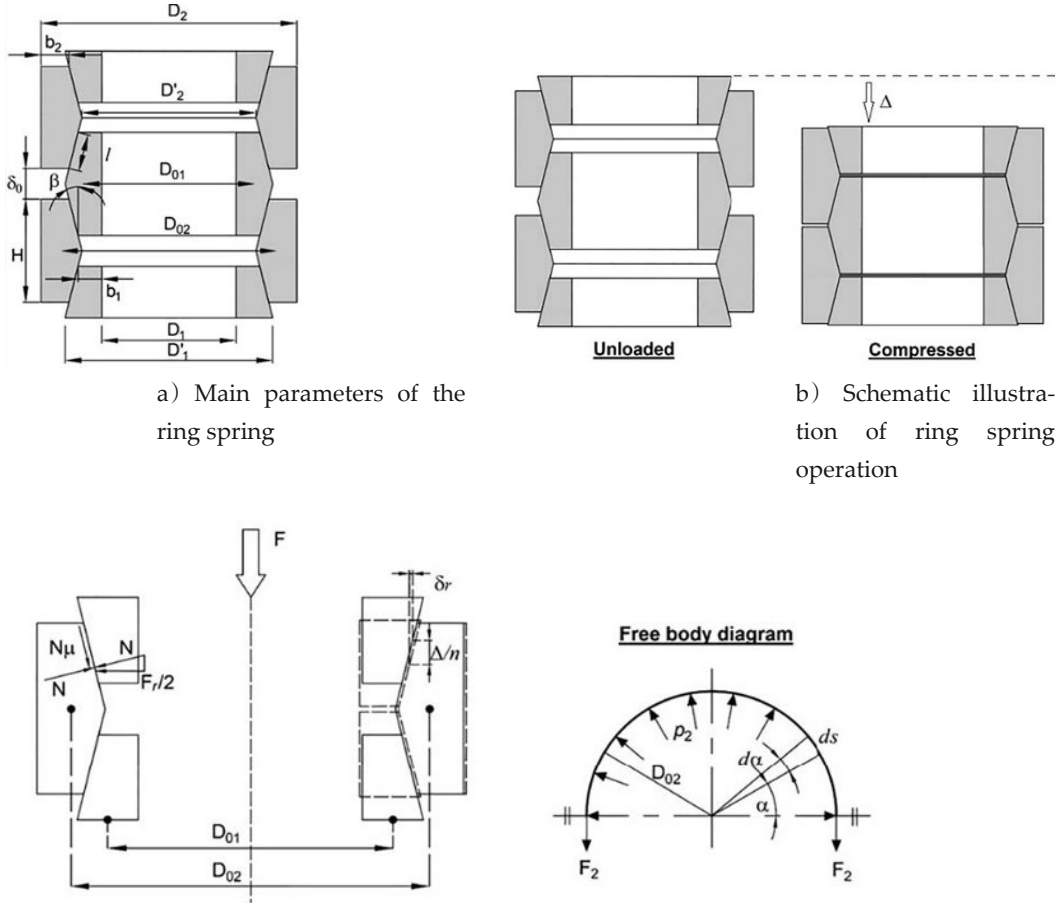

a) Main parameters of the ring spring

b) Schematic illustration of ring spring operation

c) Schematic illustration of the forces acting on the ring spring

Figure 3 Schematic illustration of the configuration and working mechanism of the SMA ring springs

With the above stiffness calculation method for SMA ring springs, a constitutive model relating the force and displacement of the SMA ring springs can be established. This model comprises mainly a skeleton curve and a hysteresis rule.

https://doi.org/10.59238/j.pt.XXXX.XX.001

The skeleton curve of the precompressed SMA ring springs is shown in Figure 4 and includes six main control points, namely, O, A, B, C, D, and E.

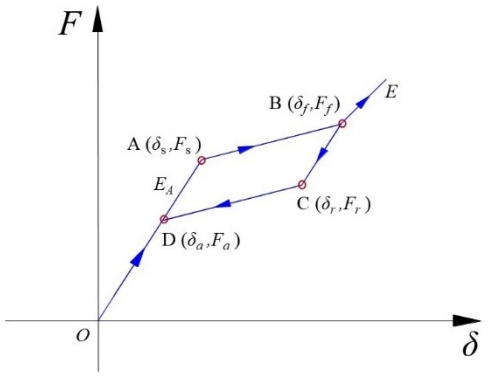

Figure 4 Constitutive model of force versus displacement for the SMA ring springs

As the core self-centering component of the rocking bridge, the constitutive model of the SMA ring springs comprises primarily a five-stage skeleton curve, as shown in Figure 4. The OA segment represents the perfectly elastic working stage, during which no relative slip occurs at the contact interface between the inner and outer rings, and only elastic deformation is observed. After the AB segment is reached, relative slip between the inner and outer rings is initiated. If loading continues beyond point B, the inner ring becomes locked by the outer ring, and the stress-hardening stage BE is entered, where the stiffness approaches infinity. The unloading segment BC constitutes the friction reversal stage, where the strain level does not change significantly but the stress level decreases rapidly because of friction reversal. If unloading continues, the response follows the CD segment, with a stiffness that is significantly lower than that at the BC stage. Further unloading leads to the DO segment, where reverse friction disappears, corresponding to the elastic recovery stage under precompression. In fact, each complete unloading cycle results in a small residual displacement, which is negligible. By default, the stress state of the SMA ring springs returns to zero. This constitutive model fully accounts for the superelastic effect of SMA materials and satisfactorily captures the self-recovery behavior after compression unloading. On the basis of the working mechanism of the SMA ring springs, a mathematical description of the hysteresis rule of the constitutive model is provided in Equation (14), and the relevant parameters can be determined through experiments and numerical simulations.

$$\begin{cases} K\delta, & 0 \le \delta < \delta_s \\ F_s + (F_f - F_s)\left(\dfrac{\delta - \delta_s}{\delta_f - \delta_s}\right), & \delta_s \le \delta < \delta_f \\ F_f + (F_r - F_f)\left(\dfrac{\delta - \delta_f}{\delta_r - \delta_f}\right), & \delta_r \le \delta < \delta_f \\ F_r + (F_a - F_r)\left(\dfrac{\delta - \delta_r}{\delta_a - \delta_r}\right), & \delta_a \le \delta < \delta_r \end{cases} \tag{14}$$

where K is the initial elastic modulus, and $A(\delta_s, F_s)$, $B(\delta_f, F_f)$, $C(\delta_r, F_r)$, and $D(\delta_a, F_a)$ denote the displacement and force coordinates of the four skeleton points.

2.3 Tension–Compression Quasistatic Tests of the SMA Ring Springs

To verify the correctness of the above constitutive model, quasistatic tests were conducted for the SMA ring springs [27]. The tested SMA ring spring specimen comprised 16 SMA outer rings (made of 38CrMoAl steel), 15 precision steel inner rings (made of Q235 steel), and one half inner ring at each end. The detailed dimensions of the outer rings, inner rings, and half inner rings are shown in Figure 5. Assuming a friction coefficient of 0.1 at the interface between the inner and outer

rings, the total compression capacity of the specimen is 42.5 mm. Via the use of the equations in Section 2.2, the predicted yield point, loading stiffness, and unloading stiffness of the ring spring were 104 kN, 2.6 kN/mm, and 1.08 kN/mm, respectively. On the basis of these values, the skeleton points of the constitutive model of the SMA ring springs were determined. The loading protocol adopted in the quasi-static test is shown in Figure 6.

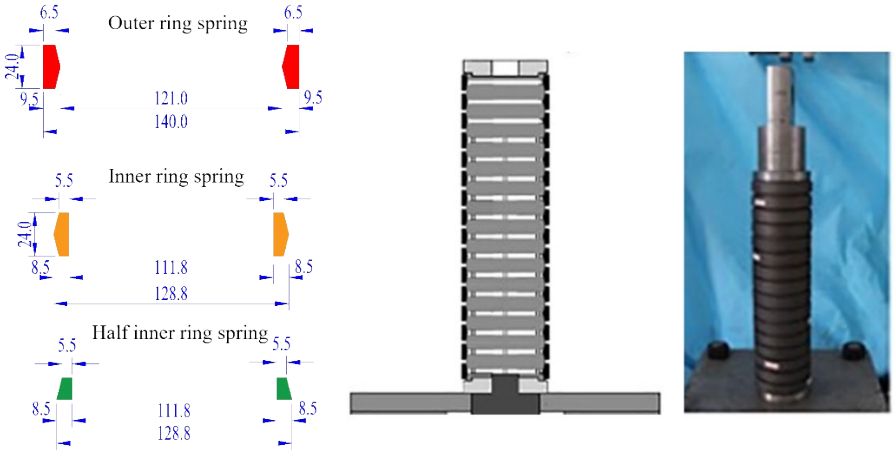

Figure 5 SMA ring spring specimen and its dimensions（units：mm）

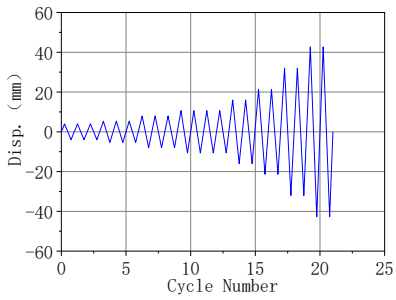

Figure 6 Loading protocol for the SMA ring spring specimen

Via the use of the constitutive model proposed in Section 2.2, numerical simulations were conducted for the SMA ring spring specimen shown in Figure 5. The experimental and simulation results are shown in Figure 7, and satisfactory agreement between the two sets of results can be observed, thus demonstrating that the proposed constitutive model is correct.

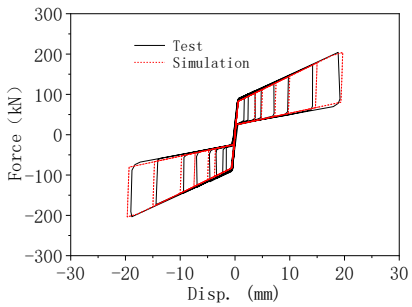

Figure 7 Comparison of the experimental and simulation results for the SMA ring springs

2.4 Design Criteria and Method for SMA Ring Spring Rocking Piers

During the design of the rocking pier, three working conditions should be considered, namely, minor, moderate, and major earthquakes. Under minor earthquakes, to ensure that no uplift occurs at the rocking interface, a certain preload must be applied to the SMA ring spring assemblies. Under moderate earthquakes

 https://doi.org/10.59238/j.pt.XXXX.XX.001

(E1), uplift of the rocking pier is permitted, but the maximum horizontal slip ratio at the pier top must not exceed 1.0%. Under major earthquakes (E2), the pier is not required to yield, and the maximum horizontal slip ratio should not exceed 2.5%. The iterative design procedure for the SMA ring spring rocking pier is shown in Figure 8.

(1) First, the geometric parameters of the pier, such as the radius r and the longitudinal reinforcement ratio ρ, are determined preliminarily.

(2) The horizontal load F_E at the pier top is estimated on the basis of the design response spectrum. Multiplying F_E by the pier height h_1 provides the bending moment M_E at the pier base. If M_E exceeds the yield moment M_Y of the pier base, the cross-sectional dimensions or reinforcement ratio should be adjusted until M_E approaches M_Y. Once the yield moment of the RC pier base is determined, the rocking moment (αM_Y) can be obtained. The rocking moment parameter α can be determined by Equation (15).

$$\alpha = \frac{h_1 + h_2 + e}{h_1} \tag{15}$$

(3) On the basis of the limit value of the horizontal slip ratio, the total horizontal displacement (δ) induced by both the deformation of the pier and rigid-body rotation at the onset of yielding, the maximum uplift distance (e) of the upper cap, and the restoring forces provided by the SMA ring springs (e.g., $F_{\mathrm{SMA-1}}$ and $F_{\mathrm{SMA-2}}$) can be determined. In accordance with the magnitude of the restoring forces, the structural dimensions of the SMA ring springs are designed.

(4) It is then verified whether the slip ratio at the pier top is lower than the design target of 2.5%. Otherwise, the iterative design process is restarted from the beginning. Notably, the slip ratio should be determined by the combined contribution of the rocking angle and the flexural deformation of the pier.

To achieve the design philosophy of no damage under minor earthquakes, replaceable damage under moderate earthquakes, and repairable damage under major earthquakes, a capacity-protected design approach is adopted for vulnerable components such as expansion joints, abutments, and pile foundations, thereby ensuring that they remain within the elastic range under major earthquakes. With respect to the rocking pier itself, a capacity-protected design concept is also applied to maintain it elastic during rocking. Replaceable elements such as bearings and SMA ring springs should be replaced only if they are damaged after an earthquake.

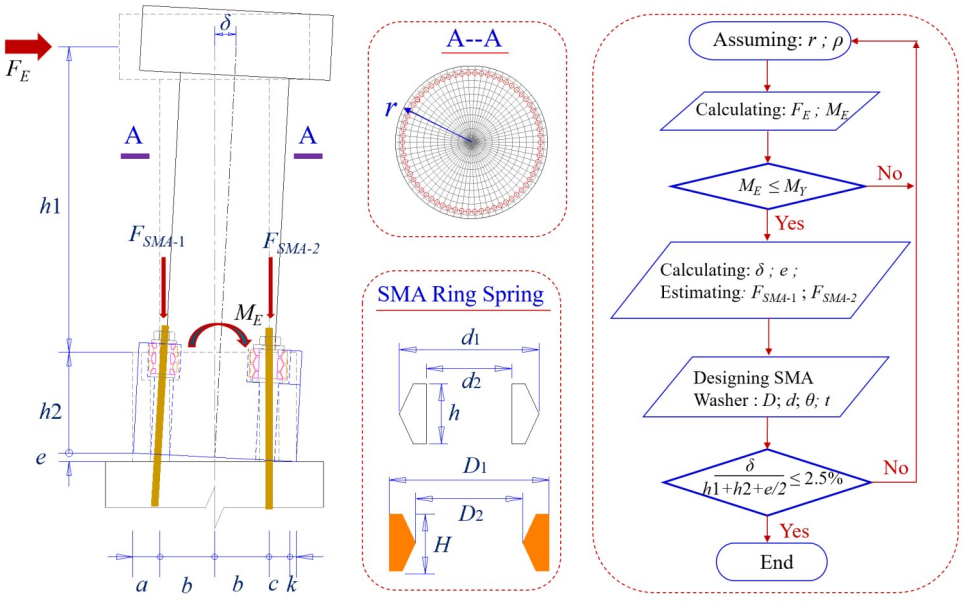

Figure 8 Flowchart of the iterative design procedure for SMA ring spring rocking piers

3 Fragility Analysis of the Rocking Bridge

3.1 Bridge Description

To verify the feasibility and effectiveness of the proposed rocking bridge, a two-span RC continuous girder bridge (20.0 m + 20.0 m) was designed. The bridge encompasses a single-column rocking pier with a height of 5.0 m and a diameter of 2.0 m. The heights of both the upper and lower caps are 2.0 m. Both the rocking pier and the caps are cast from ECC material. Each expansion joint exhibits a width of 0.22 m, and the anchorage zones are also made of ECC material to satisfy the maximum slip ratio requirement of 2.5% under major earthquakes (E2). The detailed configuration is shown in Figure 9. Two sliding bearings are arranged on each abutment, and two fixed bearings are arranged on the cap above the intermediate pier. The box girder is constructed from C50 concrete with a 28-day compressive strength of 50.0 MPa. The abutments, pier, and pile caps are constructed from C40 concrete with a 28-day compressive strength of 40.0 MPa. The diameter of the longitudinal reinforcement of the RC pier is 32.0 mm, while that of the stirrups is 16.0 mm. Their yield strengths are 440.0 and 300.0 MPa, respectively. A conventional bridge is also considered as a control group. In the conventional bridge, the height of the RC pier is 7.0 m, and the compressive strength of the concrete is 40.0 MPa. The other design parameters remain unchanged.

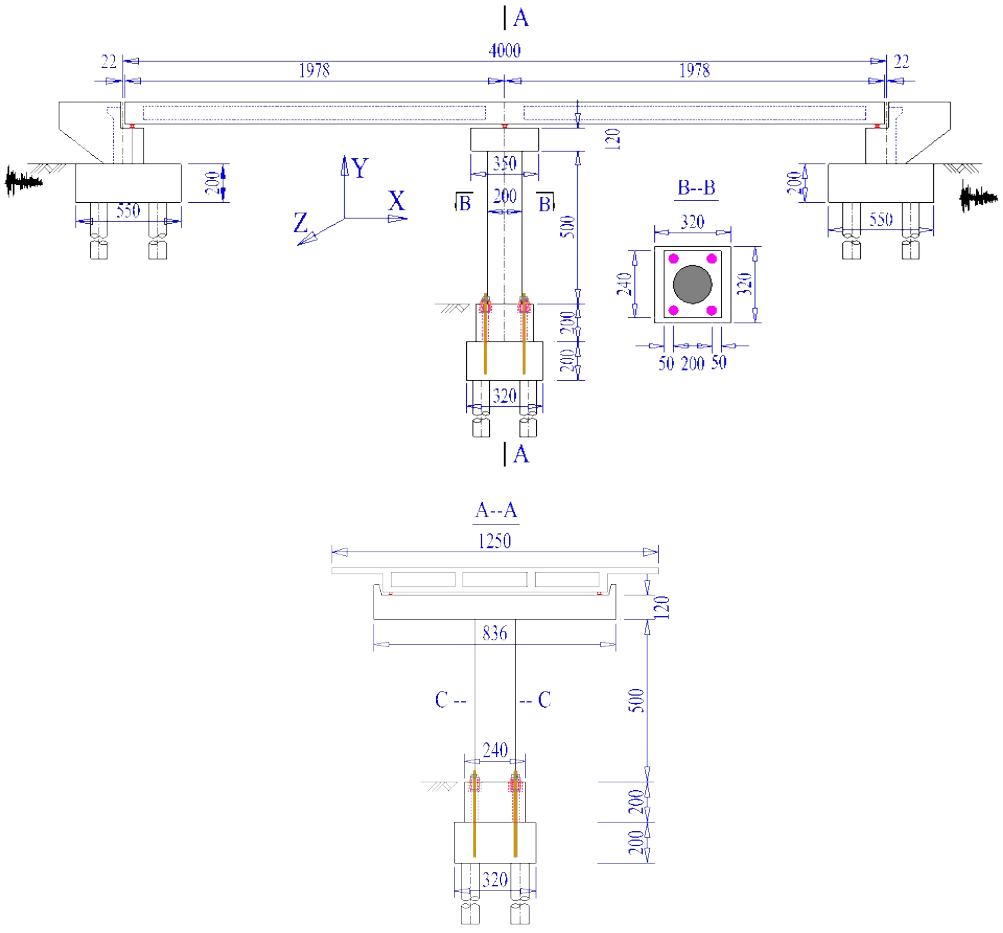

Figure 9 Configuration of the rocking bridge (unit: cm)

Following the design procedure shown in Figure 8, the final configuration of the rocking pier is obtained, as shown in Figure 9. A total of 72 longitudinal steel bars with a diameter of 32.0 mm are uniformly arranged along the longitudinal direction of the intermediate pier, resulting in a reinforcement ratio of 1.84%. The spacing between adjacent spiral stirrups is 0.12 m, and the thickness of the concrete

https://doi.org/10.59238/j.pt.XXXX.XX.001

cover of the pier is 6.5 cm. Four sets of SMA ring spring assemblies are installed. Each set comprises four pairs of ring springs connected in series. The key parameters of one SMA ring spring are shown in Figure 10. For each ring spring, the maximum deformation is 15.0 mm, and the corresponding maximum compressive load is approximately 260.0 kN. Thus, the entire SMA ring spring assembly can sustain a compressive load of 1,300.0 kN with a maximum deformation capacity of 60.0 mm.

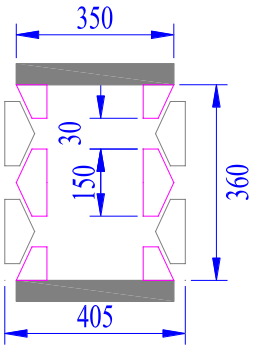

Figure 10 Schematic illustration of the SMA ring spring dimensions（units：mm）

To prevent the uplift of the interface between the upper and lower caps under normal service conditions and minor earthquakes, each SMA ring spring set is precompressed to a load of 1,080.0 kN, with a precompression deformation of 30.0 mm. The remaining deformation capacity of each SMA ring spring is 30.0 mm, which provides a maximum slip ratio of 1.2% at the pier top. Once the compressive displacement of an SMA ring spring exceeds 60.0 mm, the set becomes locked, and the maximum rocking moment at the pier base at locking is 3.762×10^4 kN·m.

3.2 Development of Nonlinear Finite Element Models of the Bridge

To compare the differences in fragility between conventional and rocking bridges, nonlinear finite element models of both bridge types were established in open-source software OpenSees. The nonlinear finite element modeling process is described using a rocking bridge as an example. The nonlinearities of the steel reinforcement and ECC material were accounted for, and the constitutive models of stress versus strain for the steel reinforcement and ECC material are shown in Figures 11 and 12, respectively [28-29]. The parameters of the constitutive model for the ECC material are listed in Table 1.

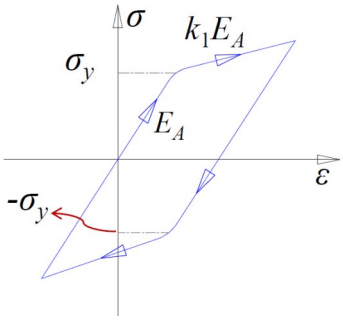

Figure 11 Stress–strain constitutive model of the steel reinforcement

The ECC pier was modeled via a fiber beam–column element based on displacement interpolation functions. The circular cross-section of the pier was uniformly discretized into 8 layers along the radial direction, and each layer was divided into 24 fiber elements along the circumferential direction. Rigid elements were employed to model the cap beam and the upper and lower caps. To capture the time-varying contact forces at the rocking pier interface, 8 pairs of zero-length contact elements were placed at the interface. The four sets of SMA ring springs

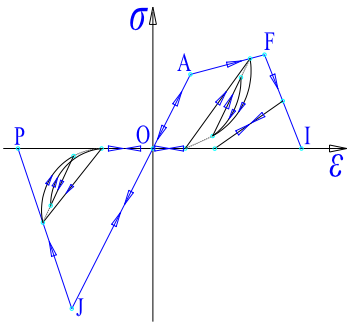

Figure 12 Stress–strain constitutive model of the ECC material

Table 1 Parameters of the constitutive model for the ECC material

Compression zone		Tension zone	
Parameter	**Value**	**Parameter**	**Value**
Cracking strength	80 MPa	Cracking strength	4.5 MPa
Cracking strain	-0.5%	Cracking strain	0.01%
Ultimate strength	0.0 MPa	Hardening strength	6.0 MPa
Ultimate strain	-2.0%	Hardening strain	3.8%
/	/	Fracture strength	0.0 MPa
/	/	Fracture strain	6.0%

were also modeled on the basis of zero-length elements, and the preload applied to the SMA ring spring assemblies was simulated by assigning an initial strain to the self-centering material. Since the main girder remains essentially elastic during earthquakes, it was modeled on the basis of elastic beam-column elements. Each expansion joint was modeled via a zero-length gap element with a joint width of 0.22 m. Each pile foundation was simulated through the use of six zero-length soil spring elements. The finite element model of the entire bridge is shown in Figure 13.

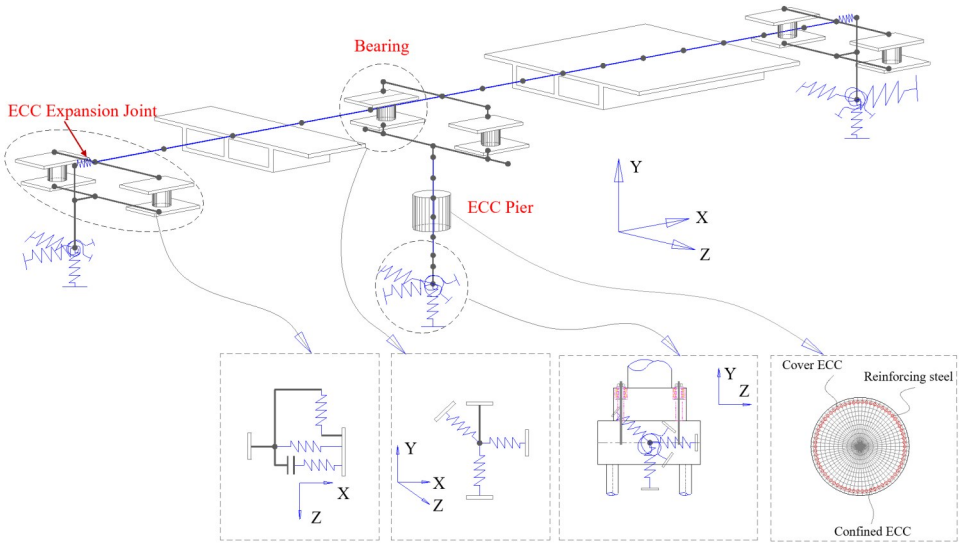

Figure 13 Finite element model of the ECC rocking bridge

3.3 Selection of Ground Motions

In fragility analysis, nonlinear time-history analysis of the structure under seismic excitations is necessary. Therefore, 52 ground motion records with different intensities were selected as external excitations in this study [30]. The acceleration response spectra of the selected ground motions are shown in Figure 14, and the probability distribution of the peak ground acceleration (PGA) is shown in

 https://doi.org/10.59238/j.pt.XXXX.XX.001

Figure 15.

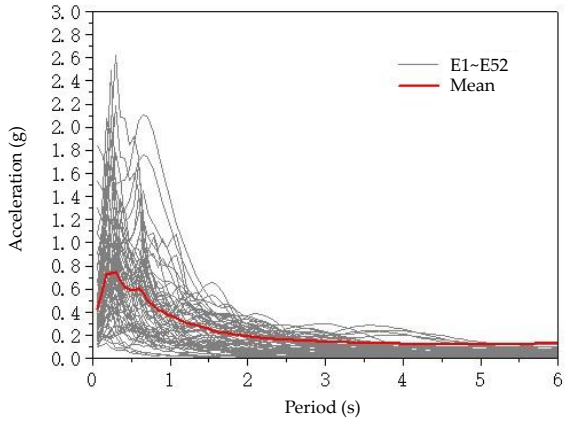

Figure 14 Acceleration response spectra of the selected ground motions

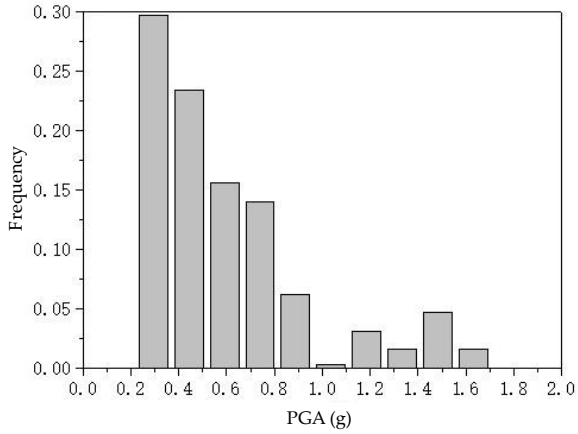

Figure 15 Histogram of the PGA frequency distributions of the selected ground motions

The selection of the intensity measure (IM) plays a crucial role in ensuring the effectiveness of fragility analysis. Common intensity measures related to ground motion include the peak ground acceleration (PGA) and peak ground velocity (PGV). According to the recommendations of Mackie and Stojadinovi [30], the linear consistency of log-probability analysis can serve as an indicator of the suitability of a given IM for interpreting results. On the basis of these criteria, both the PGA and PGV are suitable choices for IMs with respect to the engineering demand parameter (EDP). Padgett et al. [31] also evaluated various IMs in terms of efficiency, practicality, sufficiency, and hazard relevance and concluded that the PGA is a preferred IM. Therefore, the PGA was selected as the characteristic IM in this study.

3.4 Evaluation of the Performance of the ECC Material

In this study, the curvature ductility of the cross-section within the plastic hinge region at the bottom of the intermediate pier was selected as the postearthquake performance evaluation index. Among the 52 ground motion records, three ground motions with varying intensities were selected to analyze both bridge structural systems (the ECC rocking bridge and the conventional bridge with normal concrete). The moment–curvature ductility curves of the cross-section within the plastic hinge region at the pier bottom were generated. Under seismic excitation with a PGA of 0.24g, the maximum curvature ductility of the conventional RC pier reached 1.12, indicating that the pier had just yielded and entered the plastic stage. In contrast, the maximum curvature ductility of the ECC pier reached only 0.53, and the cross-section remained within the elastic range, as shown in Figure 16 a),

thus satisfying the requirement that the horizontal slip ratio at the pier top must be less than 2.5% under major earthquakes (E2). Under a PGA of 0.48g, the maximum curvature ductility levels of the conventional and rocking piers were 1.81 and 0.63, respectively, as shown in Figure 16 b). Under a PGA of 0.89g, the conventional bridge experienced damage (corresponding to a maximum curvature ductility of 2.63), whereas the cross-section of the rocking pier just entered the plastic stage (with a maximum curvature ductility of 1.23), as shown in Figure 16 c). These findings fully demonstrate that the use of ECC material can significantly improve the seismic performance of bridge piers.

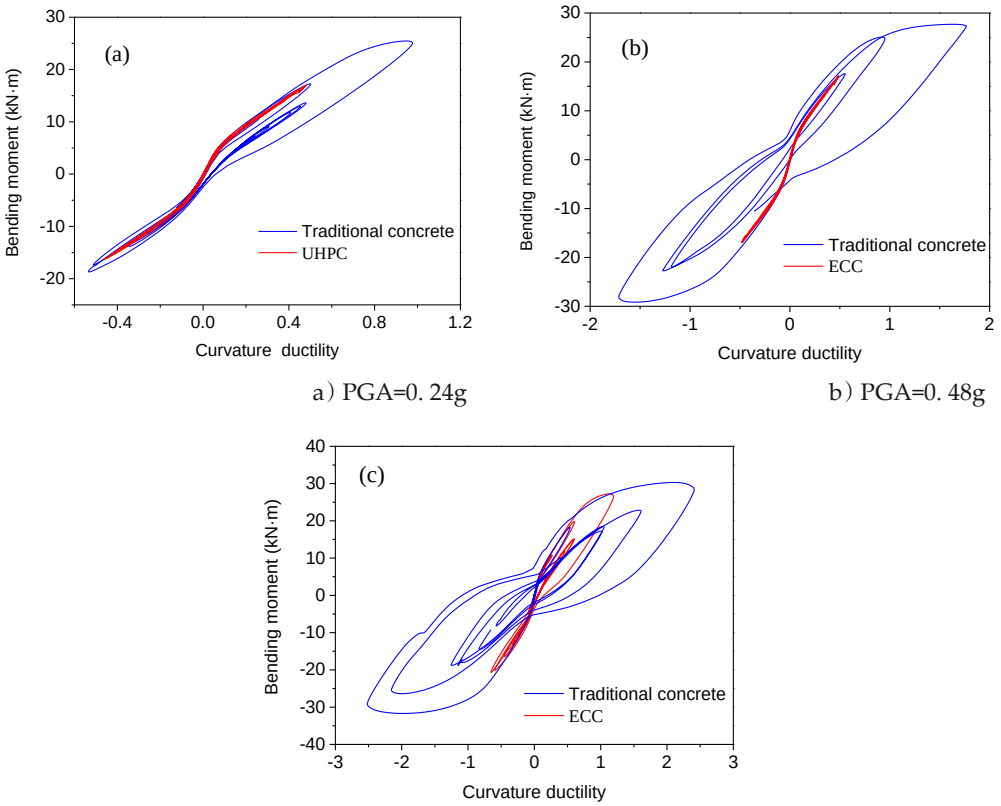

a）PGA=0. 24g b）PGA=0. 48g

c）PGA=0. 89g

Figure 16 Moment–curvature response of the pier bottom section

3.5 Fragility Analysis

In accordance with HAZUS [32] and other guidelines, four damage states (DSs) were defined, namely, slight damage, moderate damage, extensive damage, and collapse. The classification of the four damage states is related to the condition of the pier column and bearings, as detailed in Table 2. The fragility curves can be obtained from Equation (16). To evaluate the fragility of the rocking bridge, the maximum curvature ductility of the cross-section within the plastic hinge region at the pier bottom and the maximum shear strain of the bearings were selected as EDPs, with the PGA serving as the IM. Then, seismic analyses were conducted for both the conventional and rocking bridges in OpenSees, followed by regression fitting of the parameters.

$$P\left(EDP - DI_i \geq 0 | IM\right) = 1 - \varphi\left(\frac{\ln\left(\frac{DI_i}{aIM^b}\right)}{\xi_{EDP|IM}}\right) \tag{16}$$

where $\phi(\cdot)$ is the standard normal cumulative distribution function, and $\xi_{EDP|IM}$ is the standard deviation of the lognormal distribution.

https://doi.org/10.59238/j.pt.XXXX.XX.001

Table 2 Seismic damage states of the ECC pier and bearings

Bridge component	Damage index	Slight damage (DS=1)	Moderate damage (DS=2)	Extensive damage (DS=3)	Collapse (DS=4)
/	Physical description	Cracking and spalling	Moderate cracking and spalling	Performance degradation without collapse	Performance failure and collapse
Pier column	Curvature ductility	μk > 1	μk > 2	μk > 4	μk > 7
	Displacement ductility	μd > 1.0	μd > 1.2	μd > 1.76	μd > 4.76
	Slip ratio	θ > 0.007	θ > 0.015	θ > 0.025	θ > 0.050
Bearing	Maximum displacement	δ > 0 mm	δ > 50 mm	δ > 100 mm	δ > 150 mm
	Shear strain	γ > 100%	γ > 150%	γ > 200%	γ > 250%

On the basis of the analysis results, the regression coefficients *a* and *b* for the curvature ductility of the plastic hinge region of the conventional bridge pier are 4.2 and 0.638, respectively, and those for the shear strain of the bearing are 1.441 and 0.344, respectively. With respect to the rocking pier, the regression coefficients *a* and *b* are 0.67176 and 0.28826, respectively, and those for the shear strain of the bearing are 1.20173 and 0.02991, respectively. The fitting results of the pier and bearing indices versus the PGA for both bridges are shown in Figure 17. The goodness of fit of the regression coefficients and the significance results of the chi-square test are provided in Table 3. The significance level of the chi-square test is within 5%, suggesting that the confidence level for a significant relationship between the fitted results and the measured data exceeds 95%. Moreover, the goodness-of-fit R^2 values are greater than 0.6, which indicates that the fitting accuracy is acceptable.

Table 3 Seismic damage states of the ECC pier and bearings

Bridge type	Component	Fitted *a*	Std. dev. of *a*	Fitted *b*	Std. dev. of *b*	Chi-square significance level	Goodness-of-fit R^2
Conventional bridge	Pier column	4.2001	0.63334	0.6381	0.07041	4.6%	0.683
	Bearing	1.4412	0.03496	0.3442	0.03456	2.0%	0.684
Rocking bridge	Pier column	0.6717	0.01322	0.2882	0.02726	0.3%	0.698
	Bearing	1.2017	0.02991	0.4262	0.03695	1.5%	0.745

The fragility curves of the bearings in the conventional and rocking bridges are shown in Figure 18 a). The results indicated that the damage probabilities of the conventional bearing under the four damage states were greater than those of the bearing in the rocking bridge system. At a PGA of 1.0g, the probability of slight damage to the bearing in the rocking bridge system was only 75.6% of that of the conventional bridge. At a PGA of 2.0g, the probabilities of moderate damage, extensive damage, and collapse of the bearing were 81%, 35%, and 12%, respectively, of those of the conventional bridge. These findings indicate that for E1- and E2-level earthquakes, the rocking pier can effectively reduce the occurrence probability of bearing damage. The fragility curves associated with the four damage states for the RC column of the conventional pier are shown in Figure 18 b), and the fragility curves of the plastic hinge region of the pier columns for both bridge types are

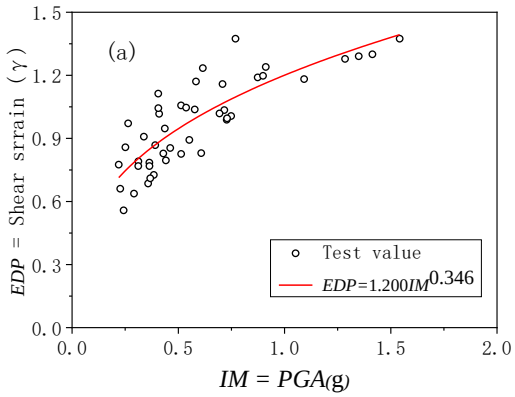

a) Conventional bridge bearing: EDP vs. IM

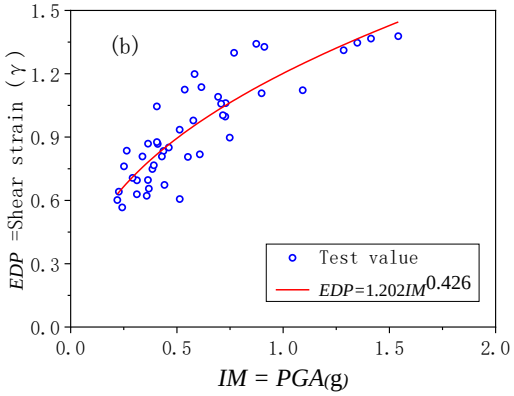

b) Rocking bridge bearing: EDP vs. IM

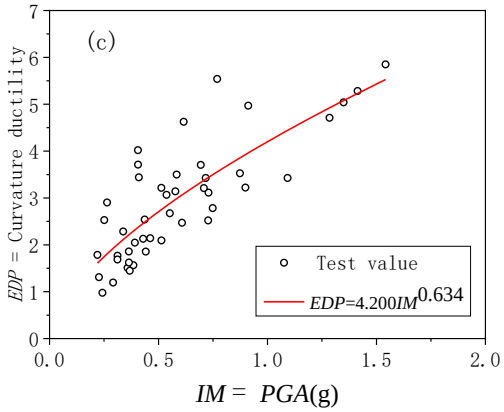

c) Conventional bridge pier: EDP vs. IM

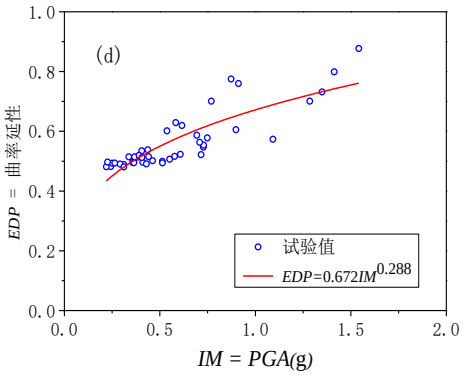

d) Rocking bridge pier: EDP vs. IM

Figure 17 Relationships between the EDP and IM for conventional and rocking bridges

shown in Figure 18 c). The results demonstrate that under a given ground motion intensity, the damage probability of the RC pier column of the conventional bridge was much greater than that of the rocking ECC pier column. Therefore, the application of a rocking bridge can greatly improve the seismic performance of the pier column.

Most researchers have considered only component-level fragility. However, since a bridge constitutes a system comprising multiple integrated components, the seismic performance of the entire structural system can be accurately evaluated only by obtaining the fragility curve of the overall bridge system. For example, Nielson and DesRoches [33] and Song and Kang [34] considered the probability of at least one component exceeding its corresponding damage state when calculating the fragility curve of a bridge system and then employed the Monte Carlo simulation method to analyze the fragility of the bridge system. However, the Monte Carlo simulation method requires substantial computational time. Moreover, under seismic action, different components of a bridge (e.g., pier and bearing) may exhibit distinct damage states, making it difficult to describe the overall damage state of the bridge system on the basis of the damage state of a single component. System fragility can be derived on the basis of postearthquake functionality or repair cost or can be jointly calculated on the basis of the fragility of individual bridge components by establishing a joint probabilistic seismic demand model.

https://doi.org/10.59238/j.pt.XXXX.XX.001

According to the relationship of each component to the overall system, the system can be simply classified as a series or parallel system for analysis. In a series system, each component is equally important to the bridge system, and each component plays an indispensable role. In this case, damage to any component results in the same level of system damage. Therefore, the overall damage state can be determined by the maximum damage state among the components as follows

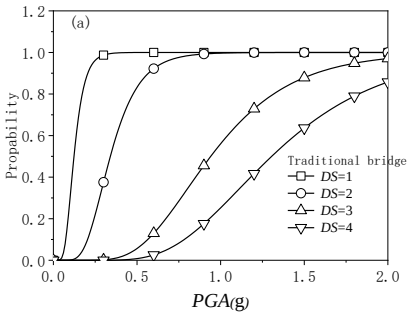

a) Fragility of the bearings in the conventional bridge

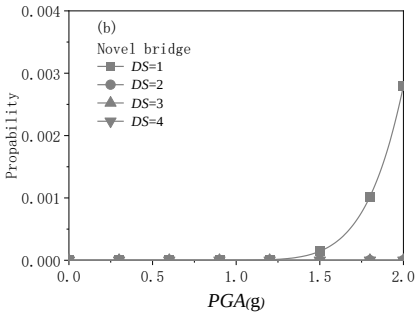

b) Fragility of the bearings in the rocking bridge

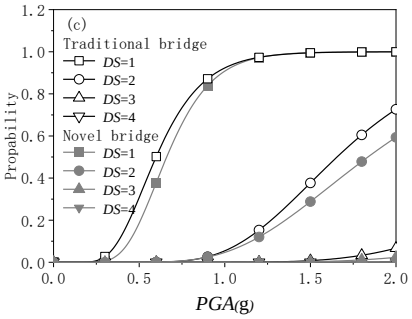

c) Fragility of the pier columns of the two bridge types

Figure 18 Fragility of the bearings and pier columns of conventional and rocking bridges

$$DS_{system} = \max\left(DS_{pier},\ DS_{bearing}\right) \tag{17}$$

Where DS_{system} is the damage state of the bridge system, DS_{pier} is the damage state of the concrete pier, and DS_{bearing} is the damage state of the bearing. Nielson and DesRoches [33] also proposed the following upper and lower bounds of the system damage state for the series system:

$$\max\left(P\left(F_i\right)\right) \le P\left(F_{system}\right) \le 1 - \prod[1 - P(F_i)] \tag{18}$$

Where $P(F_i)$ and $P(F_{\text{system}})$ denote the damage probabilities of component i and the bridge system, respectively. The upper bound is reached when all the components are completely independent. Moreover, the lower bound is achieved when all the components are perfectly correlated. Under realistic conditions, bridge system fragility occurs between these two bounds, and its exact position depends on the correlation among component effects.

In a parallel system, the functions of individual components do not interfere with each other. Hence, the bridge system reaches a given damage state only when all the components have reached that damage state. Therefore, the system damage state can be determined by the minimum damage state among the components as

follows:

$$DS_{system} = \min\left(DS_{pier},\ DS_{bearing}\right) \tag{19}$$

Similarly, the damage probability of a parallel system can be calculated by Equation (9). The upper bound is achieved when all the components are perfectly correlated. Moreover, the lower bound is reached when all the components are completely independent. The interval between the upper and lower bounds is relatively wide, which highlights the importance of the correlation among component effects for assessing the damage state of the entire system.

$$\prod[P(F_i)] \le P\left(F_{system}\right) \le \min\left(P\left(F_i\right)\right) \tag{20}$$

In reality, a bridge system is neither a pure series system nor a pure parallel system but lies in between. Moreover, the responses of individual components to seismic loading are correlated. For example, Kim et al. [35] reported that the overall seismic performance of a multispan simply supported girder bridge is significantly influenced by bearing damage. However, the bearing response is induced by both the applied loading and load transfer from other bridge components. Therefore, the coupled interactions among components should be accounted for in the overall damage state of the bridge. Consequently, the bounds given by Equations (7) and (9) can serve as a basis for assessing the damage level of a bridge system.

Given the individual fragility curves of different components, the fragility curve of the overall system can be obtained. Via the use of the system failure model proposed above, fragility curves that account for the seismic performance of both the pier and the bearing can be generated. Since the series system is more unfavorable to the structure than the parallel system is, the series model was adopted to generate system fragility curves.

As expressed in Equation (7), the fragility curve of a series system under each damage state comprises upper and lower bounds. The upper bound is expressed as the combination of the fragility levels of individual components, and the lower bound is the maximum fragility among the components. On the basis of the series model, system fragility curves for the four damage states (slight damage, moderate damage, extensive damage, and collapse) are shown in Figure 19. The fragility of the rocking bridge is generally lower than that of the conventional bridge. Notably, in the present test results, the fragility of the rocking bridge pier is much lower than that of its bearing (e.g., at a PGA of 1.8g, the fragility of the bridge pier is approximately 0.1% of the bearing damage probability). Referring to Equation (9), when the pier fragility approaches zero, the upper and lower bounds of the system fragility curve coincide. In contrast, for the conventional bridge model, under the same seismic excitation, the damage to the bridge pier is more severe than that to the bearing (e.g., at a PGA of 0.4g, the probability of slight damage to the pier is 96%, while the probability of slight damage to the bearing is only 19%). Consequently, when the series model is applied, the pier becomes the dominant factor controlling system fragility, and the theoretical upper and lower bounds of the conventional bridge system are relatively close to each other.

In this numerical simulation study, the upper and lower bounds of the two bridge systems do not strictly coincide. Choosing the slight damage state as an example, the differences between the upper and lower bounds are provided in Table 4 for seven selected PGA levels. The results reveal that the differences between the upper and lower bounds are on the order of 10^{-5}, which is negligible in engineering practice. This result suggests that when the fragility probability of one component in a series system is much lower than that of the other components, the theoretical upper and lower bounds of the system fragility curve can be considered coincident. Therefore, in this numerical simulation study, it is reasonable to assume

 https://doi.org/10.59238/j.pt.XXXX.XX.001

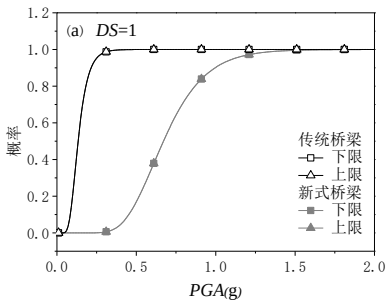

a) Fragility under slight damage

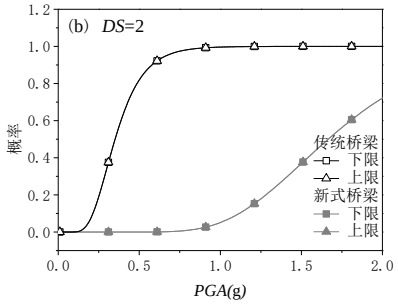

b) Fragility under moderate damage

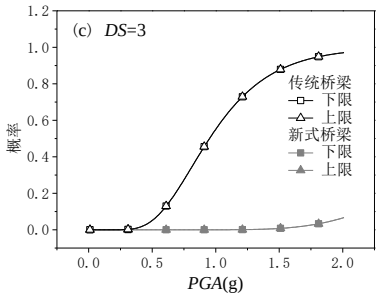

c) Fragility under extensive damage

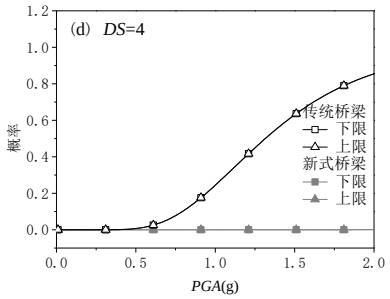

d) Fragility under collapse

Figure 19 Upper and lower bounds of fragility for conventional and rocking bridges

that the upper bound curve represents the fragility curve of the bridge system. Notably, the damage probabilities of the rocking bridge system under all four damage states are significantly lower than those of the conventional bridge system, and the difference in system fragility decreases rapidly with increasing PGA.

Table 4 Upper and lower bounds of system fragility for the slight damage state and their differences

PGA (g)	Conventional bridge (upper)	Conventional bridge (lower)	Rocking bridge (upper)	Rocking bridge (lower)	Difference
0.2	0.8610	0.8609	3.25×10^{-5}	3.25×10^{-5}	0.8601
0.4	0.9983	0.9981	0.0456	0.0456	0.9527
0.6	1.0	1.0	0.3583	0.3583	0.6417
0.8	1.0	1.0	0.7165	0.7165	0.2835
1.0	1.0	1.0	0.9024	0.9024	0.0976
1.2	1.0	1.0	0.9703	0.9703	0.0297
1.4	1.0	1.0	0.9914	0.9914	0.0086

4 Conclusions

To achieve the new seismic design philosophy of no damage under minor earthquakes, replaceable damage under moderate earthquakes, and repairable damage under major earthquakes, a self-centering rocking bridge system incorporating SMA ring springs is proposed. First, a constitutive model is developed on the basis of the results of quasistatic tests and the working mechanism of the SMA

ring springs. An iterative design method for rocking piers is subsequently proposed. Finally, finite element models of conventional and rocking bridges are established. A set of ground motions with different intensities and spectral characteristics is selected to analyze fragility at both the component and system levels. The fragility probabilities under the slight, moderate, extensive, and collapse damage states are evaluated, revealing the seismic advantages of the rocking bridge. The fragility of the bridge system is examined on the basis of series and parallel models, and the postearthquake damage state of the bridge system is quantified. The conclusions are as follows:

(1) The SMA ring springs can provide a substantial restoring force for the rocking pier. The flag-shaped constitutive model enables the SMA ring springs to simultaneously achieve self-centering and frictional energy dissipation. In applications, the deformation demand can be satisfied by adjusting the geometric dimensions, the number of units, or the assembly configuration, thereby offering convenience and flexibility.

(2) An iterative design method for SMA ring spring rocking piers is proposed, thereby ensuring that the pier remains elastic under E1- and E2-level earthquakes.

(3) The performance of the rocking bridge is similar to that of a conventional bridge under minor earthquakes, but the rocking bridge provides an effective resilience enhancement capability for E1- and E2-level earthquakes. Owing to the self-locking mechanism of the SMA ring springs, excessive horizontal displacement of the bridge can be effectively prevented.

(4) Compared with conventional bridges, rocking bridges can significantly reduce fragility under seismic loading. For example, at a PGA of 1.0g, the fragility of the rocking bridge is approximately 10% lower than that of the conventional bridge under slight damage, approximately 96% lower under moderate damage, approximately 60% lower under extensive damage, and approximately 23% lower under collapse.

Founding: The authors extended their sincere gratitude for the Shandong Hi-Speed Co., Ltd. (SDEYH-2020-04), the Qinghai Provincial Science and Technology Department project (2024-QY-202), and the scientific research project of the Guizhou Provincial Highway Bureau, the Natural Science Foundation of Shanghai (Grant No. 24ZR1472500) from Science and Technology Commission of Shanghai Municipality, Supported by Science and Technology Projects of Xizang Autonomous Region, China (Grant No. XZ202601ZY0251).

Conflict of Interest: The authors declare that there is no conflict of interest regarding the publication of this paper.

Data Availability Statement: Data Availability**Statement**: The data that support the findings of this study are available from the corresponding author upon reasonable request.

 https://doi.org/10.59238/j.pt.XXXX.XX.001

Baixian Fu
B.E. Prof. Level Senior Engineer.
Research Direction: Intelligent Operation and Maintenance of Expressways.
Email: 460504940@qq.com

Xian'gang Liu
B.E. Senior Engineer. Working at Guiyang Highway Bureau, Guizhou Province.
Research Direction: Highway Engineering Construction and Maintenance.
Email: 1241566840@qq.com

Jinglin Zhou
B.E. Engineer. Working at Guiyang Highway Bureau, Guizhou Province.
Research Direction: Highway Engineering Construction and Maintenance.
Email: 553472914@qq.com

Haifeng Shi
B.E. Engineer. Working at Wudang Highway Management Section, Guizhou Province.
Research Direction: Highway Maintenance.

Email: 43327754@qq.com

Chao Xie
B.E. Engineer. Working at Guizhou Qingzhen Highway Management Section.
Research Direction: Highway Engineering Construction.
Email: 367292420@qq.com

Qiuyue Li
B.E. Working at Guizhou Qingzhen Highway Management Section.
Research Direction: Highway Engineering Construction.

Email: 1348858626@qq.com

Yuxiao Wang
Doctoral Student. Studying at Civil Engineering College, Tongji University.
Research Direction: Bridge seismic resistance, structure health monitoring and application of new materials.
Email: wong_reshaw@tongji.edu.cn

References

1. Ministry of Transport of the People's Republic of China. JTJ 004—89 Specifications of Earthquake Resistant Design for Highway Engineering. China Communications Press: Beijing, 1989.(in Chinese)
2. American Association of State Highway and Transportation Officials. *AASHTO LRFD Bridge Design Specifications*, 3rd ed. ed.; American Association of State Highway and Transportation Officials: Washington DC, 2005.
3. Zhuang W.; Liu Z.; Jiang J. Earthquake-induced Damage Analysis of Highway Bridges In Wenchuan Earthquake and Countermeasures. *Chinese Journal of Rock Mechanics and Engineering* **2009**, 28, doi:10.3321/j.issn:1000-6915.2009.07.011.

(in Chinese)
4. Ministry of Transport of the People's Republic of China. JTG/T B02-01—2008 Specifications for Seismic Design of Highway Bridges. China Communications Press: Beijing, 2008.(in Chinese)
5. American Association of State Highway and Transportation Officials. *AASHTO LRFD Bridge Design Specifications*, 6th ed. ed.; American Association of State Highway and Transportation Officials: Washington DC, 2012.
6. Kawashima K.; MacRae G.A.; Hoshikuma J.; Nagaya K. Residual displacement response spectrum. *Journal of Structural Engineering-Asce* **1998**, 124, 523-530, doi:10.1061/(Asce)0733-9445(1998)124:5(523).
7. Federal Emergency Management Agency. *Seismic performance assessment of buildings, Volume 1 – Methodology*; FEMA P-58-1; U.S. Department of Homeland Security: 2018.
8. Japan Road Association. Design specifications of highway bridges, Part V Seismic Design. *Japan Road Association*: **2012**.
9. Hieber D.G.; Wacker J.M.; Eberhard M.O.; Stanton J.F. *Precast concrete pier systems for rapid construction of bridges in seismic regions*; WA-RD 611.1; University of Washington: Washington DC, 2005.
10. *Mander, J.B.*; Cheng, C.T. Seismic resistance of bridge piers based on damage avoidance design; NCEER-97-**0014**; University at Buffalo: 1997.
11. Pang J.B.; Steuck K.P.; Cohagen L.; Eberhard M.O.; Stanton J.F. *Rapidly constructible large-bar precast bridge-bent connection*; WA-RD 684.2; University of Washington: Washington DC, 2008.
12. Nguyen W.; Trono W.; Panagiotou M.; Ostertag C.P. *Seismic response of a hybrid fiber-reinforced concrete bridge column detailed for accelerated bridge construction* PEER 2014/19; University of California, Berkeley: 2014.
13. Cheng, C.T. Shaking table tests of a self-centering designed bridge substructure. *Engineering Structures* **2008**, 30, 3426-3433,
doi:10.1016/j.engstruct.2008.05.017.
14. Palermo A.; Pampanin S.; Marriott D. *Design*, modeling, and experimental response of seismic resistant bridge piers with posttensioned dissipating connections. Journal of Structural Engineering **2007**, 133, 1648-1661, doi:10.1061/(Asce) 0733-9445(2007)133:11(1648).
15. Pollino M.; Bruneau M. Seismic retrofit of bridge steel truss piers using a controlled rocking approach. *Journal of Bridge Engineering* **2007**, 12, 600-610, doi:10.1061/(Asce)1084-0702(2007)12:5(600).
16. Kam W.Y.; Pampanin S.; Palermo A.; Carr A.J. Self-centering structural systems with combination of hysteretic and viscous energy dissipations. *Earthquake Engineering & Structural Dynamics* **2010**, 39, 1083-1108, doi:10.1002/eqe.983.
17. Palermo A.; Pampanin S.; Calvi G.M. Concept and development of hybrid solutions for seismic resistant bridge systems. *Journal of Earthquake Engineering* **2005**, 9, 899-921, doi:10.1142/S1363246905002328.
18. Tilby, C. South Rangitikei Railway Bridge Construction. *Transactions of the New Zealand Institution of Engineers Incorporated: Civil Engineering Section* **1981**, 8, 33-48.
19. Han Q.; Jia Z.; He W.; et al. Seismic Design Method and Its Engineering Application of Self-centering Double-column Rocking Bridge. *China Journal of Highway and Transport 2017*, **30**, 169-177, doi:10.3969/j.issn.1001-7372.2017.12.018.(in Chinese)
20. DesRoches R.; Delemont M. Seismic retrofit of simply supported bridges using shape memory alloys. *Engineering Structures* **2002**, 24, 325-332, doi:10.1016/S0141-0296(01)00098-0.
21. Varela S.; Saiidi M. A bridge column with superelastic NiTi SMA and replaceable rubber hinge for earthquake damage mitigation. *Smart Materials and Structures* **2016**, 25, doi:10.1088/0964-1726/25/7/075012.
22. Ge J.P.; Saiidi M.S.; Varela S. Computational studies on the seismic response of the State Route 99 bridge in Seattle with SMA/ECC plastic hinges. *Frontiers of Structural and Civil Engineering* **2019**, 13, 149-164, doi:10.1007/s11709-018-0482-6.
23. Fang C.; Yam M.C.H.; Ma H.; Chung K.F. Tests on superelastic Ni–Ti SMA bars under cyclic tension and direct-shear: towards practical recentring connections. *Materials and Structures* **2013**, 48, 1013-1030, doi:10.1617/s11527-013-0212-4.
24. Qiu C.X.; Fang C.; Liang D.; Du X.L.; Yam M.C.H. Behavior and application of self-centering dampers equipped with buckling-restrained SMA bars. *Smart Materials and Structures* **2020**, 29, doi:10.1088/1361-665X/ab6883.
25. Zouatine M.; Helm L.; Sadegh-Azar H. Seismic performance and design of an innovative structure with controlled rocking shear wall using ring springs. *Soil Dynamics and Earthquake Engineering* **2024**, 185, doi: 10.1016/j. soildyn.2024.108911.
26. Engelke C.F.; Helm L.; Sadegh-Azar H. Experimental study on the displacement- and frequency-dependency of ring

springs under dynamic loads. *Structures* **2026**, 85, doi:10.1016/j.istruc.2026.111181.
27. Wang W.; Fang C.; Zhao Y.S.; Sause R.; Hu S.L.; Ricles J. Self-centering friction spring dampers for seismic resilience. *Earthquake Engineering & Structural Dynamics* **2019**, 48, 1045-1065, doi:10.1002/eqe.3174.
28. Menegotto M.; Pinto P.E. Method for analysis of cyclically loaded reinforced concrete plane frames including changes in geometry and non-elastic behavior of elements under combined normal force and bending. *In Proceedings of the Proceedings of IABSE Symposium on Resistance and Ultimate Deformability of Structures Acted on by Well-Defined Repeated Loads*, Lisbon, 1973.
29. Zhang N.; Gu Q.; Dong Y.; Qian J.; Zheng Y. Seismic performance of bridges with ECC-reinforced piers. *Soil Dynamics and Earthquake Engineering* **2021**, 146, doi:10.1016/j.soildyn.2021.106753.
30. Mackie K.R.; Stojadinović B. Fragility basis for California highway overpass bridge seismic decision making; 2005/02; Pacific Earthquake Engineering Research Center, University of California, Berkeley: 2005.
31. Padgett J. E.; Nielson B. G.; DesRoches R. Selection of optimal intensity measures in probabilistic seismic demand models of highway bridge portfolios. *Earthquake Engineering & Structural Dynamics* **2007**, 37, 711-725, doi: 10.1002/eqe.782.
32. Federal Emergency Management Agency. *Multi-hazard loss estimation methodology earthquake model: Technical manual*; U. S. Department of Homeland Security: Washington, D.C, 2003.
33. Nielson B.G.; DesRoches R. Seismic fragility methodology for highway bridges using a component level approach. *Earthquake Engineering & Structural Dynamics* **2007**, 36, 823-839, doi:10.1002/eqe.655.
34. Song J.; Kang W.H. System reliability and sensitivity under statistical dependence by matrix-based system reliability method. *Structural Safety* **2009**, 31, 148-156, doi:10.1016/j.strusafe.2008.06.012.
35. Kim S.H.; Mha H.S.; Lee S.W. Effects of bearing damage upon seismic behaviors of a multi-span girder bridge. *Engineering Structures* **2006**, 28, 1071-1080, doi:10.1016/j.engstruct.2005.11.015. AUTHOR BIOGRAPHIES